

COMPARISON OF ALGORITHMS FOR DETERMINATION OF ROTATION MEASURE AND FARADAY
STRUCTURE I. 1100 - 1400 MHZX. H. SUN¹, L. RUDNICK², TAKUYA AKAHORI¹, C. S. ANDERSON¹, M. R. BELL³, J. D. BRAY⁴, J. S. FARNES¹, S.
IDEGUCHI⁵, K. KUMAZAKI⁵, T. O'BRIEN², S. P. O'SULLIVAN¹, A. M. M. SCAIFE⁴, R. STEPANOV^{6,7}, J. STIL⁸, K.
TAKAHASHI⁹, R. J. VAN WEEREN¹⁰, M. WOLLEBEN⁸*To appear in AJ*

ABSTRACT

Faraday rotation measures (RMs) and more general Faraday structures are key parameters for studying cosmic magnetism and also are sensitive probes of faint ionized thermal gas. There is a need to define what derived quantities are required for various scientific studies, and then to address the challenges in determining Faraday structures. A wide variety of algorithms have been proposed to reconstruct these structures. In preparation for the Polarization Sky Survey of the Universe's Magnetism (POSSUM) to be conducted with the Australian Square Kilometre Array Pathfinder (ASKAP) and the ongoing Galactic Arecibo L-band Feeds Array Continuum Transit Survey (GALFACTS), we run a Faraday structure determination data challenge to benchmark the currently available algorithms including Faraday synthesis (previously called RM synthesis in the literature), wavelet, compressive sampling and QU -fitting. The input models include sources with one Faraday thin component, two Faraday thin components and one Faraday thick component. The frequency set is similar to POSSUM/GALFACTS with a 300-MHz bandwidth from 1.1 to 1.4 GHz. We define three figures of merit motivated by the underlying science: a) an average RM weighted by polarized intensity, RM_{wtd} , b) the separation $\Delta\phi$ of two Faraday components and c) the reduced chi-squared χ_r^2 . Based on the current test data of signal to noise ratio of about 32, we find that: (1) When only one Faraday thin component is present, most methods perform as expected, with occasional failures where two components are incorrectly found; (2) For two Faraday thin components, QU -fitting routines perform the best, with errors close to the theoretical ones for RM_{wtd} , but with significantly higher errors for $\Delta\phi$. All other methods including standard Faraday synthesis frequently identify only one component when $\Delta\phi$ is below or near the width of the Faraday point spread function; (3) No methods, as currently implemented, work well for Faraday thick components due to the narrow bandwidth; (4) There exist combinations of two Faraday components which produce a large range of acceptable fits and hence large uncertainties in the derived single RMs; in these cases, different RMs lead to the same Q, U behavior, so no method can recover a unique input model. Further exploration of all these issues is required before upcoming surveys will be able to provide reliable results on Faraday structures.

Subject headings: polarization — ISM: magnetic fields — magnetic fields — radio continuum: general — techniques: polarimetric

1. INTRODUCTION

Cosmic magnetism is one of the key science projects for the future Square Kilometre Array (SKA), which will measure Faraday rotation measures (RMs) of tens of mil-

lions of background radio sources to reveal how cosmic magnetic fields are generated and how they evolve over cosmic time (Gaensler *et al.* 2004). It is therefore crucial to appropriately define and determine RMs, which can be very challenging when a radio source has more than a single Faraday component, which we will hereinafter designate as a composite Faraday structure. A source can be identified as being a Faraday composite if its fractional linear polarization is not constant as a function of wavelength squared (λ^2).

Faraday rotation occurs when a linearly polarized radio wave propagates in a magneto-ionic medium. In the simplest case, the polarization angle is rotated by an amount proportional to the wavelength squared, providing the definition of RM as

$$\chi(\lambda^2) = \chi_0 + RM\lambda^2, \quad (1)$$

where $\chi(\lambda^2)$ is the polarization angle observed at λ^2 and χ_0 is a constant. The RM in the simple case of a foreground screen is proportional to the integral of thermal electron density multiplied by magnetic field parallel to the line of sight from the source to the observer. A posi-

¹ Sydney Institute for Astronomy, School of Physics, The University of Sydney, NSW 2006, Australia; x.sun@physics.usyd.edu.au

² Minnesota Institute for Astrophysics, School of Physics and Astronomy, University of Minnesota, 116 Church Street SE, Minneapolis, MN 55455, USA; larry@umn.edu

³ Max Planck Institute for Astrophysics, Karl-Schwarzschild-Str. 1, 85748 Garching, Germany

⁴ Department of Physics & Astronomy, University of Southampton, Highfield, Southampton SO17 1BJ, UK

⁵ University of Nagoya, Furo-cho, Chikusa-ku, Nagoya 464-8601, Japan

⁶ Institute of Continuous Media Mechanics, Korolyov str. 1, 614061 Perm, Russia

⁷ Perm National Research Polytechnic University, Komsomolskii Av. 29, 614990 Perm, Russia

⁸ Department of Physics and Astronomy, University of Calgary, 2500 University Drive NW, Calgary AB T2N 1N4, Canada

⁹ University of Kumamoto, 2-39-1, Kurokami, Kumamoto 860-8555, Japan

¹⁰ Harvard-Smithsonian Center for Astrophysics, 60 Garden Street, Cambridge, MA 02138, USA

tive RM indicates a magnetic field pointing towards the observer.

RMs of background *compact* extragalactic radio sources have been used to study magnetic fields in Galactic objects such as H II regions (Harvey-Smith *et al.* 2011), high velocity clouds (Hill *et al.* 2013), and supernova remnants (Sun *et al.* 2011). On larger scales, they are used to probe magnetic fields in the Galaxy (Han *et al.* 1997; Sun and Reich 2010; Wolleben *et al.* 2010; Pshirkov *et al.* 2011; Van Eck *et al.* 2011; Jansson and Farrar 2012; Akahori *et al.* 2013), in nearby (Han *et al.* 1998; Gaensler *et al.* 2005; Mao *et al.* 2012) and in high redshift galaxies (Bernet *et al.* 2013). On yet larger scales, RM probes have been used for galaxy clusters including embedded radio galaxies (Bonafede *et al.* 2013) and are proposed for cosmic webs (Akahori and Ryu 2010, 2011; Akahori *et al.* 2014).

Most of the currently available RMs were obtained by linearly fitting polarization angles versus λ^2 over a narrow range. For example, the catalog by Taylor *et al.* (2009) containing 37 543 RMs was based on polarization angles at 1364.9 MHz and 1435.1 MHz from the NRAO VLA Sky Survey (Condon *et al.* 1998). However, the linear relation between polarization angle and λ^2 is violated when a radio source has multiple Faraday components or Faraday depolarization effects occur, and RMs from the linear fit of polarization angle versus λ^2 are not reliable (Farnsworth *et al.* 2011; O’Sullivan *et al.* 2012). Although the influence of an individual RM error for studying foreground magnetic fields can be largely eliminated with a sufficiently dense RM grid, variances in RMs can still remain. These variances are hard to interpret and can confuse measurements of small scale Faraday structure, as well as the information on the sources’ intrinsic Faraday structures. A more sophisticated understanding of RMs and development of algorithms to determine them are certainly necessary.

RMs of *diffuse* polarized emission have also been used to study the magnetic field in supernova remnants (Kothes and Brown 2009; Harvey-Smith *et al.* 2010; Sun *et al.* 2011), in the Galaxy (Haverkorn *et al.* 2003; Schnitzeler *et al.* 2009) and nearby galaxies (Braun *et al.* 2010; Fletcher *et al.* 2011; Mao *et al.* 2012). The RM structure of the radio galaxy Centaurus A indicates the existence of faint ionized thermal gas in its radio lobes (O’Sullivan *et al.* 2013). Specific Faraday signatures can manifest the helical structure of the magnetic field (Brandenburg and Stepanov 2014; Horellou and Fletcher 2014). The diffuse emission is usually modeled as a slab with a uniform mixture of synchrotron-emitting and Faraday-rotating plasmas (Burn 1966). In this case, not only the RM but also the Faraday extent of a slab are essential to properly understand the source structures. A single RM derived by fitting polarization angles versus λ^2 is unable to represent the distribution of RMs within the slab (Sokoloff *et al.* 1998). To recover the complete Faraday structure of the diffuse emission, more advanced methods are required.

Recently, there has been considerable progress in Faraday structure determination capabilities. Many observational facilities such as the Very Large Array (VLA), the Australian Telescope Compact Array (ATCA), the LOw Frequency ARray (LOFAR), the Murchison Wide-

field Array (MWA), and the Giant Metrewave Radio Telescope (GMRT) are now equipped with multi-channel broadband polarimeters which significantly reduces the ambiguities in characterizing source polarization properties.

There are large-scale surveys underway such as the Galactic Magneto-Ionic Medium Survey (GMIMS, Wolleben *et al.* 2010) and the Galactic Arecibo L-band Feeds Array Continuum Transit Survey (GALFACTS, Taylor and Salter 2010), and surveys to be conducted before the full SKA such as the Polarization Sky Survey of the Universe’s Magnetism (POSSUM, Gaensler *et al.* 2010) with the Australian SKA Pathfinder (ASKAP). These surveys aim to advance our understanding on magnetism by dissecting the Faraday structure of the magneto-ionic medium. It is therefore crucial to decide which algorithms should be applied to the dataset to produce a reliable interpretation.

Motivated by the need for competitive algorithms to reconstruct Faraday structures and the advent of many methods, we initiated a data challenge aiming to benchmark all the current methods. In this first step, we focus on the POSSUM and GALFACTS configurations, and use a similar frequency range covering 300 MHz from 1.1 to 1.4 GHz. The band is split into 300×1 -MHz channels. This paper is organized as follows. We introduce the algorithms which were included in the data challenge in Sect. 2, describe the construction of the suite of tests in Sect. 3, present the benchmark results in Sect. 4, discussions in Sect. 5, and conclusions in Sect. 6.

2. ALGORITHMS

Following Burn (1966), the observed complex-valued polarized intensity at λ^2 , $P(\lambda^2)$, can be written as

$$P(\lambda^2) = Q(\lambda^2) + iU(\lambda^2) = \int_{-\infty}^{\infty} F(\phi) \exp(2i\phi\lambda^2) d\phi. \quad (2)$$

Here ϕ , the Faraday depth, is defined as

$$\phi = K \int_{\vec{r}} n_e \vec{B} \cdot d\vec{l}, \quad (3)$$

where K is a constant, \vec{r} is the position of emission inside a source, n_e is the electron density, \vec{B} is the magnetic field and $d\vec{l}$ is the distance increment along the line of sight, and $F(\phi)$, the Faraday spectrum (previously called Faraday dispersion function), represents the complex-valued polarized intensity at ϕ . For a simple source that has polarized emission only at ϕ_0 , the Faraday spectrum is $F(\phi) = F_0 \delta(\phi - \phi_0)$, where $F_0 = f_0 \exp(2i\chi_0)$ with f_0 being the polarized intensity at zero wavelength. The observed complex-valued polarized intensity is thus $P(\lambda^2) = f_0 \exp[2i(\chi_0 + \phi_0\lambda^2)]$, and in this simple case $\text{RM} = \phi_0$. $F(\phi)$ is the key quantity that many techniques aim to extract from observations, in order to study the structure of the magneto-ionic medium.

The methods that are included in the data challenge either a) are open-ended, i.e. decomposing the Faraday spectra into some basis functions, and include Faraday synthesis (previously called RM synthesis, Brentjens and de Bruyn 2005; Bell and Enßlin 2012; Kumazaki *et al.* 2014) with Faraday clean (previously called RM clean, Heald 2009), wavelet (Frick *et al.*

TABLE 1
NOMENCLATURE.

Term	Previous names	Description
Rotation Measure		RM, defined by Equation (1)
Faraday depth		ϕ , defined by Equation (3)
Faraday spectrum	Faraday dispersion function ^a	$F(\phi)$, the complex-valued linearly polarized flux as a function of ϕ
Faraday synthesis	RM synthesis ^a	The process of deriving $F(\phi)$ from $P(\lambda^2)$ with a Fourier transform.
Faraday Point Spread Function	RM spread function ^b	FPSF, the Fourier transform of the weighting function in the λ^2 domain.
Faraday clean	RM clean ^b	The process of deconvolving an observed $F(\phi)$ into an input one using the “clean” technique
3D Faraday synthesis	Faraday synthesis ^c	Performing a 3D Fourier transform of complex-valued visibility data from the (u,v,λ^2) space to the (x,y,ϕ) space

NOTE. — ^a Brentjens and de Bruyn (2005); ^b Heald (2009); ^c Bell and Enßlin (2012)

2010, 2011) and compressive sampling (Li *et al.* 2011; Andreut *et al.* 2012) or b) assume models of the synchrotron-emitting and Faraday rotating medium to fit the observed $P(\lambda^2)$, *viz.* QU -fitting (Farnsworth *et al.* 2011; O’Sullivan *et al.* 2012; Ideguchi *et al.* 2014). When reporting the results many of the techniques involved a search by human eyes to determine whether some features in $F(\phi)$ are real.

Note that there are various terms in the literature used to describe the polarization and Faraday properties of sources, and the processes and products of transforming from observations of the Stokes parameters as a function of wavelength into a Faraday depth space. Although these terms have historical value, they are becoming increasingly discordant with the actual applications, and are often misused. In this paper, and as a suggestion to the community moving forward, we adopt the terminology described in Table 1.

2.1. Open-ended methods

2.1.1. Faraday synthesis

The complex-valued polarized intensity $P(\lambda^2)$ and the Faraday spectrum $F(\phi)$ are a Fourier transform pair from Eq. (2). Because, in practice, there are neither observations at $\lambda^2 < 0$ nor at all $\lambda^2 > 0$, the inverse Fourier transform of $P(\lambda^2)$, $\widetilde{F}(\phi)$, is actually a convolution of the true Faraday spectrum $F(\phi)$ and the Faraday Point Spread Function (FPSF, previously called RM spread function, see Table 1) $R(\phi)$ which is the Fourier transform of the weighting function $W(\lambda^2)$. The weighting function depends on the frequency band coverage and weights of each of the individual frequency channels. Brentjens and de Bruyn (2005) have given a detailed description and also presented several formulae that can be easily applied to observations, as below

$$\begin{aligned}
 \widetilde{F}(\phi) &\equiv F(\phi) \star R(\phi) \\
 &= \mathcal{K} \sum W(\lambda_i^2) P(\lambda_i^2) \exp[-2i\phi(\lambda_i^2 - \lambda_0^2)] \\
 R(\phi) &= \mathcal{K} \sum W(\lambda_i^2) \exp[-2i\phi(\lambda_i^2 - \lambda_0^2)] \\
 \lambda_0^2 &= \mathcal{K} \sum W(\lambda_i^2) \lambda_i^2 \\
 \mathcal{K} &= (\sum W(\lambda_i^2))^{-1},
 \end{aligned} \tag{4}$$

where the sums are made over all the frequency channels, λ_i^2 is the wavelength squared of each channel, λ_0^2 is the weighted average of λ_i^2 and \mathcal{K} is the normalization constant. For the current data challenge, the weighting function is $W(\lambda^2) = 1$ for $\lambda_{\min}^2 < \lambda^2 < \lambda_{\max}^2$ and $W(\lambda^2) = 0$ elsewhere. We refer to the methods employing the above formulae as the standard Faraday synthesis.

Three quantities can be used to characterize the limitations of recovering the Faraday spectrum from observations with a given frequency setup: the full width at half maximum (FWHM) of the FPSF, or equivalently, the resolution in Faraday depth space $\Delta\phi_{\text{FPSF}}$, the maximal Faraday depth ϕ_{\max} , and the largest Faraday depth scale to which the method is sensitive, $\delta\phi$. Following Brentjens and de Bruyn (2005), these quantities are determined by the minimum wavelength squared λ_{\min}^2 , the maximum wavelength squared λ_{\max}^2 and the interval of wavelength squared $\delta\lambda^2$ fixed by the channel width in frequency for the observations as

$$\begin{aligned}
 \Delta\phi_{\text{FPSF}} &= \frac{2\sqrt{3}}{\lambda_{\max}^2 - \lambda_{\min}^2} \\
 |\phi_{\max}| &= \frac{\sqrt{3}}{\delta\lambda^2} \\
 \delta\phi &= \frac{\pi}{\lambda_{\min}^2}.
 \end{aligned} \tag{5}$$

Note that ϕ_{\max} refers to Faraday thin components and $\delta\phi$ refers to Faraday thick components. For the frequency setup of the test data, the values of λ_{\min}^2 , λ_{\max}^2 , $\delta\lambda^2$, $\Delta\phi_{\text{FPSF}}$, ϕ_{\max} , and $\delta\phi$ are listed in Table 2.

TABLE 2
THE WAVELENGTH RANGE AND SEVERAL KEY PARAMETERS FOR THE DATA CHALLENGE.

λ_{\min}^2	$4.6 \times 10^{-2} \text{ m}^2$
λ_{\max}^2	$7.4 \times 10^{-2} \text{ m}^2$
$\delta\lambda^2$	$6.6 \times 10^{-5} \text{ m}^2$
$\Delta\phi_{\text{FPSF}}$	122 rad m^{-2}
$ \phi_{\max} $	26319 rad m^{-2}
$\delta\phi$	68 rad m^{-2}

A deconvolution method similar to the “clean-algorithm” widely used for radio synthesis images proposed by Högbom (1974) was developed by Heald (2009), which we refer to as the standard Faraday clean (Table 1). The method first searches for the peak in $|\widehat{F}(\phi)|$, and then subtracts the FPSF, $R(\phi)$, multiplied by the peak attenuated by a loop gain factor from $\widehat{F}(\phi)$. The process iterates until the residual $|\widehat{F}(\phi)|$ reaches a threshold or the number of loops exceeds a certain value. The clean components are then convolved to a Gaussian with a FWHM of $\Delta\phi_{\text{FPSF}}$ and added back to the residuals to form the best estimate of $F(\phi)$.

We denote a method based on Faraday synthesis and Faraday clean by “FS-” followed by the abbreviation of the respective participant’s name.¹¹ Among the algorithms, FS-JF, FS-KK, FS-LR, and FS-RvW use a standard Faraday synthesis and Faraday clean described as above; FS-MW first bins the data to achieve uniform sampling in λ^2 ; FS-MB first regrid the data so that it is equally spaced in λ^2 and applies a Fast Fourier Transform to calculate $\widehat{F}(\phi)$; FS-MBm is the same as FS-MB but with an extra step to determine the number of clean components with a maximum likelihood analysis (Bell *et al.* 2013).

2.1.2. Wavelets

The wavelet decomposition of the Faraday spectrum $F(\phi)$ into wavelet coefficients $w(a, \phi)$ can be performed by the transformation of the polarized intensity $P(\lambda^2)$ as suggested by Frick *et al.* (2010)

$$w(a, \phi) = \frac{1}{\pi} \int_{-\infty}^{\infty} P(\lambda^2) \exp(-2i\phi\lambda^2) \hat{\psi}^*(-2a\lambda^2) d\lambda^2, \quad (6)$$

where $\hat{\psi}$ is the Fourier transform of the analyzing wavelet, a defines the scale, and ϕ is the Faraday depth of the wavelet center. The Faraday spectrum $F(\phi)$ can be synthesized using the inverse transform

$$F(\phi) = \frac{1}{C_\psi} \int_{-\infty}^{\infty} \int_{-\infty}^{\infty} \psi\left(\frac{\phi-b}{a}\right) w(a, b) \frac{da db}{a^2} \quad (7)$$

where b is the position of the wavelets, and $C_\psi = 1$ for the typically chosen wavelet, the so-called “Mexican hat” $\psi(\phi) = (1 - \phi^2) \exp(-\phi^2/2)$.

The wavelet-based algorithm used here allows a combination of the Faraday Synthesis procedure and the wavelet filtering. Coefficients $w(a, \phi)$ in Eq. (7) are not necessarily the same as those obtained from Eq. (6), because there can be some additional constraints to filter an extraneous signal, such as a noise, or to complement a signal using specific assumptions (e.g. Frick *et al.* 2011). Another general purpose of the wavelet application is to provide a multi-scale structure analysis. Coefficients $w(a, \phi)$ represent a spectral composition of $F(\phi)$ locally in Faraday space and its distribution over recognizable scales, set by the wavelength range of a specific radio telescope (Beck *et al.* 2012). The advantage

of wavelet decomposition can be considerable when the range of recognizable scales in Faraday space is sufficiently wide, which means a large ratio of maximum to minimum wavelengths, namely $(\lambda_{\text{max}}/\lambda_{\text{min}})^2 \gg 1$. The current data challenge only allows for a maximum scale separation up to 1.6. This is not ideal, but is slightly above the principal scale resolution of the wavelets (typically estimated as 1.3). Therefore, wavelet analysis is possible, but cannot produce optimal results over the 1100 – 1400 MHz band tested here. For a simple source, the wavelet method gives the same result as Faraday synthesis (e.g. Frick *et al.* 2011). We refer to this method as Wavelet-RS.

2.1.3. Compressive sampling

In this method, it is assumed that the Faraday spectrum $F(\phi)$ can be represented by a sparse sample in a set of analysis functions, namely $\mathbf{f} = \mathbf{Z}\xi$, where $\mathbf{f} = \{f_1, f_2, \dots, f_M\}^T$ is the Faraday spectrum, \mathbf{Z} is the $M \times M$ transform matrix for the representation, and $\xi = \{\xi_1, \xi_2, \dots, \xi_M\}^T$ is the coefficient. The reconstruction of the Faraday spectrum then turns to the minimization problem

$$\min \sum_{m=1}^M |\xi_m| \quad \text{subject to} \quad |\mathbf{Y}\mathbf{f} - \mathbf{P}|^2 \leq (\beta\sigma)^2, \quad (8)$$

where $Y_{nm} = \exp(2i\phi_m\lambda_n^2)$ is the matrix translating the Faraday spectrum to the observed complex-valued polarized intensity $\mathbf{P} = \{P_1, P_2, \dots, P_N\}^T$, σ is the noise in Q and U in each frequency channel, $\beta = \sqrt{N}$, $m = 1, 2, \dots, M$ and $n = 1, 2, \dots, N$, where M is the number of sparse samples and N is the number of frequency channels.

The two methods used in the data challenge that are based on compressive sampling are: CS-XS developed by Li *et al.* (2011) using the Daubechies D8 wavelet transforms, and CS-JS devised by Andreut *et al.* (2012) using a boxcar and δ -function dictionary. Note that for some tests, only the δ -function library was used and the decision of which function basis to use was made based on the growth plots (all the top row grayscale plots in Andreut *et al.* 2012).

2.2. Model fitting

The QU -fitting method selects a number of independent Faraday components to produce a net $Q(\lambda^2)$ and $U(\lambda^2)$ versus λ^2 followed by a minimization procedure. A detailed description of the physical models used in QU -fitting has been given by e.g. Sokoloff *et al.* (1998), Farnsworth *et al.* (2011) and O’Sullivan *et al.* (2012). Depending on the relative distribution of synchrotron-emitting and Faraday-rotating plasmas as well as the distribution of Faraday depths, the models that are used in the current data challenge can be categorized as follows. Note that composite structures based on $F(\phi)$ are also possible, but not included in the current tests.

- **Simple Faraday screen**, where a synchrotron emitting region lies behind a Faraday rotating screen. The polarized intensity is then

$$P(\lambda^2) = p \exp[2i(\chi + \phi\lambda^2)] \quad (9)$$

¹¹ AS=Anna Scaife; JF=Jamie Farnes; JS=Jeroen Stil; KK=Kohei Kumazaki; LR=Lawrence Rudnick; MB=Michael Bell; MW=Maik Wolleben; RS=Rodion Stepanov; RvW=Reinout van Weeren; SO’S=Shane O’Sullivan; TO’B=Tim O’Brien and XS=Xiaohui Sun

If there are a small number of separate synchrotron emitting regions, then

$$P(\lambda^2) = p_1 \exp [2i(\chi_1 + \phi_1 \lambda^2)] + p_2 \exp [2i(\chi_2 + \phi_2 \lambda^2)] + \dots \quad (10)$$

- **Slab**, which represents a mixture of thermal and non-thermal plasmas. The synchrotron emissivity is uniform and the Faraday depth either increases or decreases linearly along the line of sight. The Faraday depth of the front edge of the screen is ϕ_0 and the extent of the screen in Faraday depth is ϕ_s . The expected polarized intensity can be written as

$$P(\lambda^2) = p_0 \frac{\sin(\phi_s \lambda^2)}{\phi_s \lambda^2} \exp \left[2i(\chi_0 + \phi_0 \lambda^2 + \frac{1}{2} \phi_s \lambda^2) \right] \quad (11)$$

The *QU*-fitting methods try to fit one or more of the above models to the observed $Q(\lambda^2)$ and $U(\lambda^2)$ versus λ^2 with various optimization schemes. The *QU*-fitting methods used for this data challenge are: *QU-AS*, using Markov Chain Monte Carlo with Metropolis-Hasting sampler and Bayesian evidence to distinguish between one-component and two-component models, as described by Scaife and Heald (2012); *QU-TO'B*, using least-squared fits and *QU-SO'S*, using maximum likelihood. For *QU-TO'B* and *QU-SO'S*, standard Faraday synthesis and Faraday clean are run first to provide initial values for the parameters. To distinguish between different models, *QU-SO'S* implements a Bayesian information criterion to penalize models with more parameters, while *QU-TO'B* starts with the simplest models, and then adds more parameters only if the reduced chi-squared goes down.

3. CONSTRUCTION OF THE DATA CHALLENGE

The data challenge is run for a suite of test data, where each test is a simulated data set containing 300 values of total intensity I_ν , Stokes Q_ν and U_ν for each frequency ν , where $\nu = 1.100, 1.101, 1.102, \dots, 1.399$ GHz. The total intensity is arbitrary. For polarization, we derived Q_ν and U_ν from an input model of $F(\phi)$ according to Eq. (2), and then added Gaussian random noise with $\sigma_\nu = 1$ to each of Q_ν and U_ν . The rms noise for the full band is thus $\sigma = \sigma_\nu / \sqrt{N}$, where $N = 300$ is the number of channels. The signal-to-noise ratio (SNR) was set to be $10^{1.5} \approx 32$, which is well above the expected detection threshold of 8σ for POSSUM (George *et al.* 2012). This ensures that all the methods described in Sect. 2 should be able to easily detect the signals. In practice, $q_\nu = Q_\nu / I_\nu$ and $u_\nu = U_\nu / I_\nu$ were provided instead of Q_ν and U_ν as most of the algorithms could use them to remove the influence of any non-zero spectral indices which might complicate the Faraday clean process (see Brentjens and de Bruyn 2005, for a detailed discussion).

Finally, 17 data sets were constructed for the benchmark test and they are listed in Table 5. These data cover three types of input models for the Faraday spectrum as follows:

- *One Faraday thin component*. The Faraday spectrum is simply a δ -function, $F(\phi) = F_0 \delta(\phi - \phi_0)$, where ϕ_0 is randomly selected from 5 to

500 rad m⁻² and $\text{SNR} = |F_0|/\sigma \approx 32$. This corresponds to the Faraday screen model with only one component in Sect. 2.2. The fractional polarized intensity is constant over λ^2 and the polarization angle is linearly related to λ^2 . An example (Model 1, Table 5) is shown in Fig. 1. Pulsars and some extragalactic radio sources are in this category.

- *Two Faraday thin components*. The Faraday spectrum is written as $F(\phi) = F_1 \delta(\phi - \phi_1) + F_2 \delta(\phi - \phi_2)$, where the ratio of the amplitudes is between 0.35 and 0.95 and the strong component has an SNR of 32, $0^\circ \leq |\chi_1 - \chi_2| < 180^\circ$, and $15 \text{ rad m}^{-2} \leq |\phi_1 - \phi_2| \leq 140 \text{ rad m}^{-2}$. The separations of the two components in Faraday depth for the various tests were both less than and greater than $\Delta\phi_{\text{FPSF}} \approx 122 \text{ rad m}^{-2}$. Minter and Spangler (1996) measured RMs across 23 extended radio sources around Galactic latitude $|b| = 20^\circ$ and found an rms scatter of $\sim 4 \pm 0.6 \text{ rad m}^{-2}$ on angular scales $\sim 1.2'$. This agrees with the results from a sample of 208 double sources with separations less than $3'$ at $|b| > 25^\circ$ from Rudnick *et al.* (2014, in preparation), who found a median difference of $\sim 4 \text{ rad m}^{-2}$ between lobes. We therefore included small values of $|\phi_1 - \phi_2|$, such as 14 rad m^{-2} for Model 11 in Table 5, even though they are less than the width of the FPSF. In the current tests, the Faraday depth separation is about 14 rad m^{-2} for Model 11, 40 rad m^{-2} for Models 5, 6, 8, and 9, 80 rad m^{-2} for Models 7 and 13, 140 rad m^{-2} for Models 4 and 10, and 180 rad m^{-2} for Model 12 (Table 5). We did not choose the models specifically to represent situations with RM ambiguities (e.g. Kumazaki *et al.* 2014). The spectral indices ($I_\nu \propto \nu^{-\alpha}$) are either the same for the two components, or set to $\alpha_1 = 0$ and $\alpha_2 = 0.7$, with an assumption that each component has a constant fractional polarization as a function of λ^2 . This model represents, e.g., an unresolved double source such as a radio galaxy with either two lobes or one core and one jet, each with its own Faraday screen. The polarized intensity and polarization angle can be calculated from Eq. (10). An example (Model 4, Table 5) is shown in Fig. 1.

- *Faraday thick component*. The Faraday spectrum is described by a boxcar function: $F(\phi) = F_0$ for $\phi_c - \phi_s/2 < \phi < \phi_c + \phi_s/2$; $F(\phi) = 0$ elsewhere. Here ϕ_c is the central Faraday depth of the component, ϕ_s is the Faraday depth extent of the component, and $\text{SNR} = |F_0| \times \phi_s / \sigma \approx 32$. This corresponds to the slab model described in Sect. 2.2, where ϕ_0 is either $\phi_c + \phi_s/2$ or $\phi_c - \phi_s/2$. The values of ϕ_s were 25 and 50 rad m^{-2} , both less than the maximum scale of 68 rad m^{-2} , although for the latter case there will still be strong depolarization at the lower frequencies. The thick component approximately depicts a source with both a synchrotron-emitting and Faraday rotation medium, such as Galactic diffuse emission, supernova remnants and nearby galaxies. In reality, the distribution of polarized emission is probably more extended than that of thermal gas, and thus

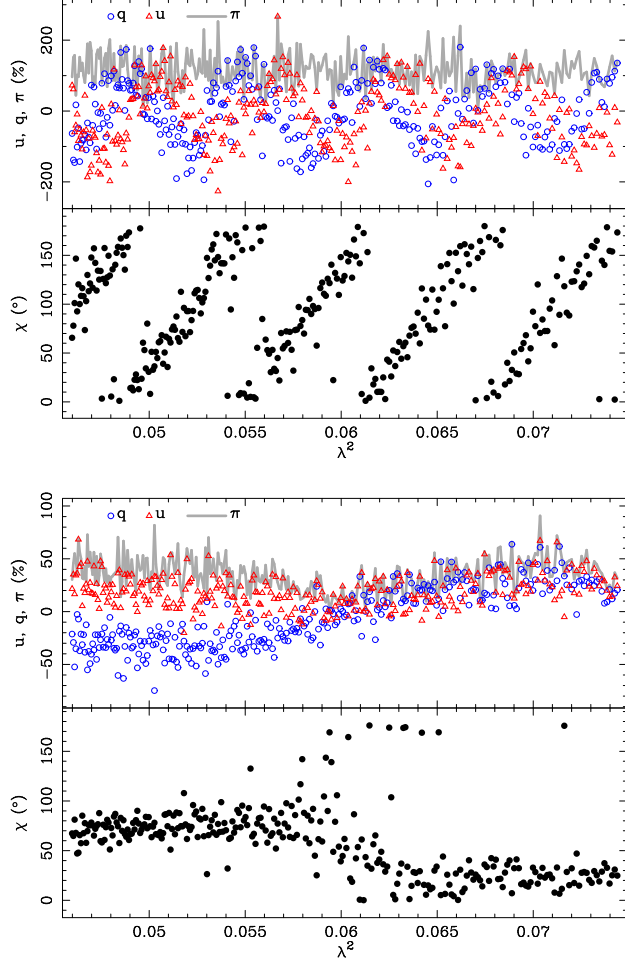


FIG. 1.— Examples of benchmark test data with input $F(\phi)$ based on one Faraday thin component (upper, Model 1 in Table 5) and based on two Faraday thin components with $\Delta\phi = 141 \text{ rad m}^{-2}$ (lower, Model 4 in Table 5). The red triangles display $u = U/I$, blue circles display $q = Q/I$, grey lines display $\pi = \sqrt{u^2 + q^2}$ and the dots display polarization angles. The point-to-point scatter reflects the noise added to each point.

the Faraday spectra can deviate substantially from a boxcar shape (Beck *et al.* 2012). An example (Model 14, Table 5) is shown in Fig. 2. In addition, three of the tests included both a Faraday thin and Faraday thick component.

4. BENCHMARK RESULTS

4.1. Overall performances of all the methods

All the results from the data challenge are listed in Table 5. We first define three quantities as figures of merit to assess these results. All of these quantities are driven by the science goals of POSSUM (Gaensler *et al.* 2010).

The first figure of merit is how well the weighted average of Faraday depth, defined as

$$\text{RM}_{\text{wtd}} = \frac{\sum_i |F_i| \phi_i}{\sum_i |F_i|}, \quad (12)$$

where i denotes different components, meets that of the input model. This is motivated by the science goal of using an RM grid to study foreground magnetic fields. Ideally, sources with only one Faraday thin component are

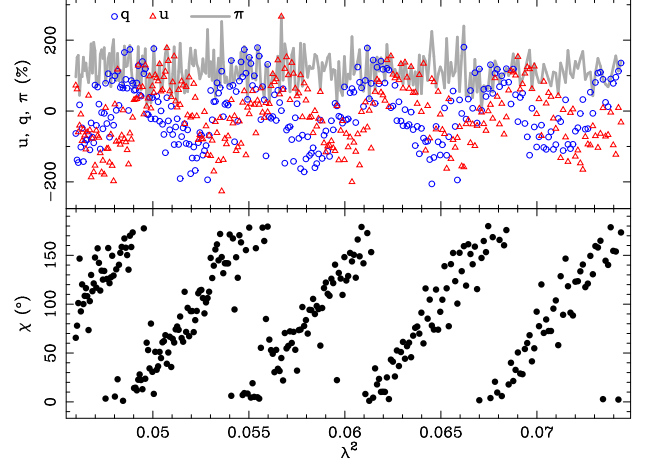


FIG. 2.— The same as Fig. 1 but for the Faraday thick model with a Faraday depth extent $\phi_s = 25 \text{ rad m}^{-2}$ (Model 16 in Table 5).

best suited for this purpose, in which case $\text{RM}_{\text{wtd}} = \text{RM}$. Sources with more Faraday thin components or Faraday thick components can also be used at the risk of increasing the scatter between the RMs. The average is weighted by polarized intensity because in the limit that the two components are not well-resolved in Faraday space, it is similar to the average result that one would get from fitting a single component to the data. The best single component fit in any individual case also depends on the relative phase (namely the difference of polarization angles) of the two input components. The theoretical error (1σ uncertainty) of the Faraday depth for a component from the Faraday synthesis method can be written as $\sigma_{\text{RM}} = 0.5 \Delta\phi_{\text{FPSF}} / \text{SNR}$, which was previously used by e.g. Mao *et al.* (2010) and has been verified by us with Monte-Carlo simulations. In the current tests, $\text{SNR} = 32$, the theoretical error is thus about 1.9 rad m^{-2} . For RM_{wtd} the error depends on the relative amplitudes of the components and is between $\sigma_{\text{RM}}/\sqrt{2}$ and σ_{RM} . For the discussions below we simply use σ_{RM} for comparison with the results. The expected median of $|\text{RM}_{\text{wtd}}(\text{test} - \text{model})|$ and the error of the median are then about $0.675\sigma_{\text{RM}} \approx 1.3 \text{ rad m}^{-2}$ and $\sigma_{\text{RM}}/\sqrt{N_{\text{test}}} \approx 0.5 \text{ rad m}^{-2}$, respectively. Here $N_{\text{test}} = 17$ is the number of tests.

The second figure of merit is the comparison between the fit and model values of the separation of the two Faraday thin components or the width of a Faraday thick component, calculated as

$$\Delta\phi = |\phi_1 - \phi_2|. \quad (13)$$

If there is only one Faraday thin component, we define $\Delta\phi = 0$. For a source with two Faraday thin components, $\Delta\phi$ measures the Faraday depth difference between these two components, which is an indicator of the thermal environment local to or inside the source. The ability to measure $\Delta\phi$ is crucial for exploring magnetic fields in the cosmic web (Akahori *et al.* 2014). For a source with a Faraday thick component, such as Galactic diffuse polarized emission, $\Delta\phi = \phi_s$ (Table 5), can be modelled in terms of a rough spatial scale of the structure particularly towards high Galactic latitudes. The fit value for $\Delta\phi$ also indicates whether a method is able to recognize the complexity of $F(\phi)$ and avoid some of the RM ambi-

guities (Farnsworth *et al.* 2011; Kumazaki *et al.* 2014).

For the second figure of merit, we therefore list for each method the difference between the model inputs and test outputs for the separation or width $|\Delta\phi(\text{test} - \text{model})|$. The theoretical error can be estimated as $\sigma_{\Delta\phi} = \sqrt{2}\sigma_{\text{RM}} \approx 2.7 \text{ rad m}^{-2}$, assuming that the two components do not interfere with each other in the Faraday spectrum. The theoretical median of $|\Delta\phi(\text{test} - \text{model})|$ and the error of the median are about $0.675\sigma_{\Delta\phi} \approx 1.8 \text{ rad m}^{-2}$ and $\sigma_{\Delta\phi}/\sqrt{N_{\text{test}}} \approx 0.7 \text{ rad m}^{-2}$, respectively. Since only the strong component has an SNR 32, the theoretical median of $|\Delta\phi(\text{test} - \text{model})|$ is slightly lower than the true value.

The last figure of merit is the reduced chi-squared χ_r^2 calculated as

$$\chi_r^2 = \frac{1}{2N - 3N_c} \sum_{i=1}^N \frac{[(\tilde{U}_i - U_i)^2 + (\tilde{Q}_i - Q_i)^2]}{\sigma_i^2}, \quad (14)$$

where N is the number of frequency channels, N_c is the number of components, $\sigma_i = 1$ is the rms noise in each channel, and \tilde{U} and \tilde{Q} are model values. For $N = 300$, the expected mean of χ_r^2 is ~ 1 with a scatter of ~ 0.02 . In addition to measuring the accuracy of the fitted Faraday depth(s), χ_r^2 also checks whether polarized amplitudes and phases are properly solved, which would be important for detailed studies of individual sources.

The three figures of merit, χ_r^2 , $|\text{RM}_{\text{wtd}}(\text{test} - \text{model})|$ and $|\Delta\phi(\text{test} - \text{model})|$, for all of the methods are shown in Fig. 3. The median values for these figures of merit for each fitting procedure as well as the theoretical expectations are listed in Table 3. Although there are always outliers for each method, clear trends can be recognized for each figure of merit: (1) All the *QU*-fitting methods have $\chi_r^2 \sim 1$ and all the other methods have median values of χ_r^2 significantly larger than the expectation. *QU*-fitting allows only 3 or 6 parameters (1 or 2 Faraday components), and then minimizes χ_r^2 . The larger values of χ_r^2 for the other methods may be due to the fact that they allowed signal power to be spread over a much larger number of components, but were forced to report only the strongest 1 or 2 components, which, by themselves, would produce a poor χ_r^2 .

Note that FS-JF used the smallest sampling of 1 rad m^{-2} in the Faraday depth domain and obtained the best χ_r^2 among the Faraday synthesis methods. Further tests are needed to investigate how the sampling influences χ_r^2 . (2) Only two of the *QU*-fitting methods, QU-TO'B and QU-SO'S have a median $|\text{RM}_{\text{wtd}}(\text{test} - \text{model})|$ consistent with the (conservative) theoretical values. (3) The *QU*-fitting methods have a much smaller median $|\Delta\phi(\text{test} - \text{model})|$ than other methods. However, none of the methods can reproduce the separations of the components within the idealized theoretical errors.

Among the Faraday synthesis methods, FS-JF, FS-KK, FS-LR and FS-RvW all used similar algorithms but delivered different results. This is likely because these methods involved different processes of searching for peaks from the Faraday spectra and deciding which peaks to report, and these processes are very subjective. In the extreme case such as FS-RvW, all the components were picked out manually, as an automatic way was not

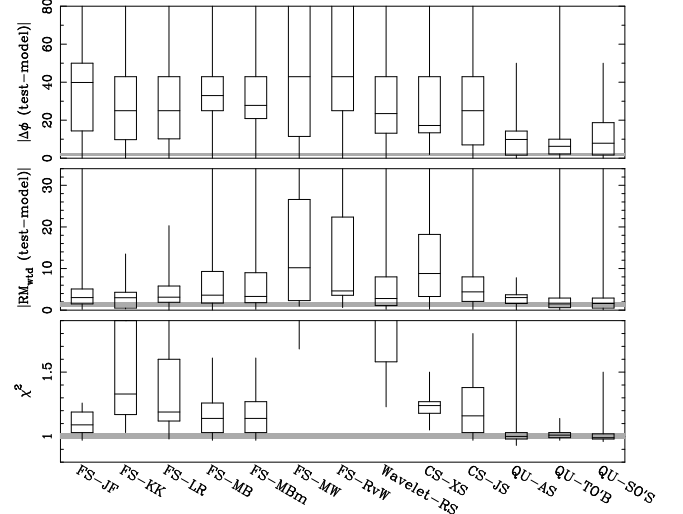


FIG. 3.— Box-and-whisker plots for figures of merit over all 17 tests. The boxes show the first, the second (median) and the third quartile, and the ends of the whiskers show the minimum and maximum values. The shaded areas indicate 1σ range above and below the theoretical medians. See Table 3 for the medians and uncertainties.

TABLE 3
MEDIAN VALUES FOR χ_r^2 , RM_{wtd} AND $\Delta\phi$ OVER ALL 17 TESTS.

Method	χ_r^2	$ \text{RM}_{\text{wtd}}(\text{test-model}) $ rad m ⁻²	$ \Delta\phi(\text{test-model}) $ rad m ⁻²
Expected	1 ± 0.02	1.3 ± 0.5	1.8 ± 0.7
FS-JF	1.09	3.0	39.9
FS-KK	1.33	3.0	25.0
FS-LR	1.19	3.1	25.0
FS-MB	1.14	3.6	33.0
FS-MBm	1.14	3.3	27.8
FS-MW	3.95	10.2	42.9
FS-RvW	...	4.6	42.9
Wavelet-RS	2.01	2.8	23.5
CS-XS	1.24	8.8	17.2
CS-JS	1.16	4.4	25.0
QU-AS	1.00	3.0	9.9
QU-TO'B	1.01	1.5	6.3
QU-SO'S	0.99	1.6	7.9

ready during the tests.

The actual science from Faraday structures usually relies on only one parameter such as RM_{wtd} or $\Delta\phi$. However, more parameters need to be fit to achieve $\chi_r^2 \sim 1$. Therefore one cannot simply differentiate all the methods solely based on χ_r^2 . For most of the methods except for *QU*-fitting, although the χ_r^2 values are much larger than 1 indicating very poor fits, the median values of $|\text{RM}_{\text{wtd}}(\text{test} - \text{model})|$ are within about 5 rad m^{-2} . These values deviate from the expectation, but are much less than the intrinsic Faraday depth fluctuations over degree scales from the Galaxy (Sun and Reich 2009; Schnitzeler 2010). This means RM_{wtd} values from these methods may still be suitable for studying magnetic fields in Galactic objects.

4.2. Fitting accuracies for different $F(\phi)$ models

We summarize here the performance of the various methods for each type of input model. For a single Faraday thin component model, most of the methods repro-

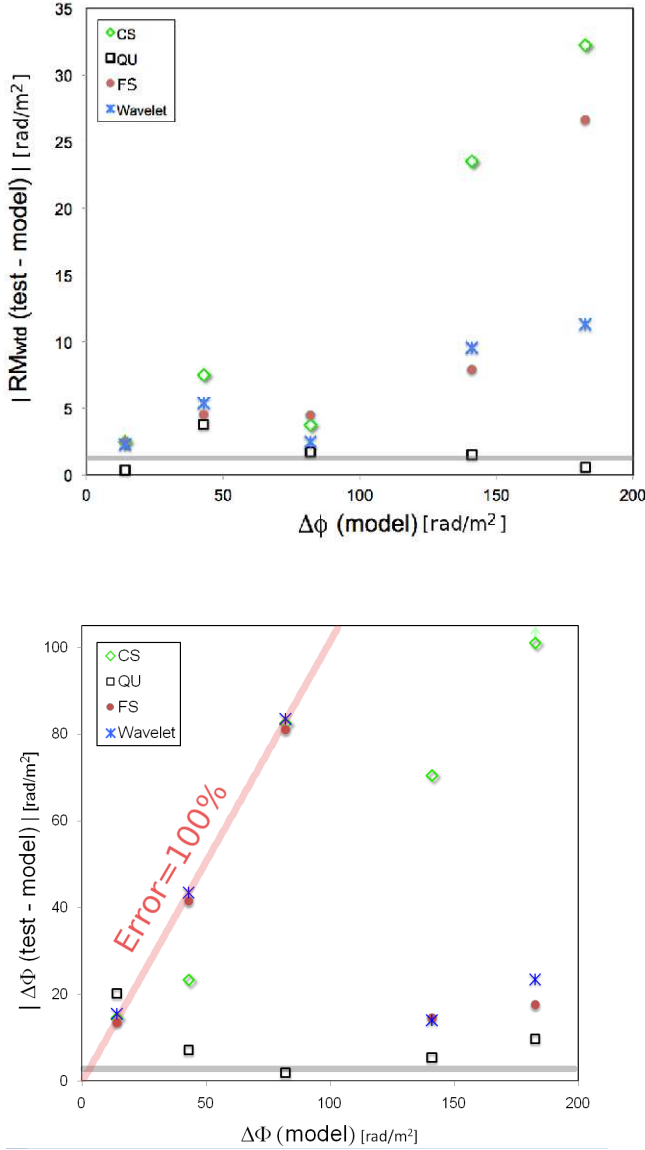


FIG. 4.— $|RM_{\text{wtd}}(\text{test} - \text{model})|$ (upper panel) and $|\Delta\phi(\text{test} - \text{model})|$ (lower panel) versus model $\Delta\phi$ for two Faraday thin components, showing the median results averaging over all algorithms of each type (Faraday synthesis, wavelets, compressive sampling and QU -fitting) and averaging all the tests with similar values of input $\Delta\phi$. The grey shaded regions at the bottom of each panel show the median expected values from the SNR alone (Table 3).

duce the inputs well. However, FS-MW and CS-XS identify more than one component for one or two cases, and FS-MW and FS-RvW obtain a too high RM_{wtd} for one case.

For two Faraday thin components, the results are much less satisfactory. Fig. 4 summarizes the results, now averaging over all algorithms of each type (Faraday synthesis, wavelets, compressive sampling, and QU -fitting). We plot the median deviations from the models as a function of the separation between the two components, $\Delta\phi$.

Looking first at $|RM_{\text{wtd}}(\text{test} - \text{model})|$, we see that *only* QU -fitting produces results that deviate from the input model approximately as expected. Somewhat surprisingly, the deviations for non- QU -fitting methods increase sharply when the separation between components

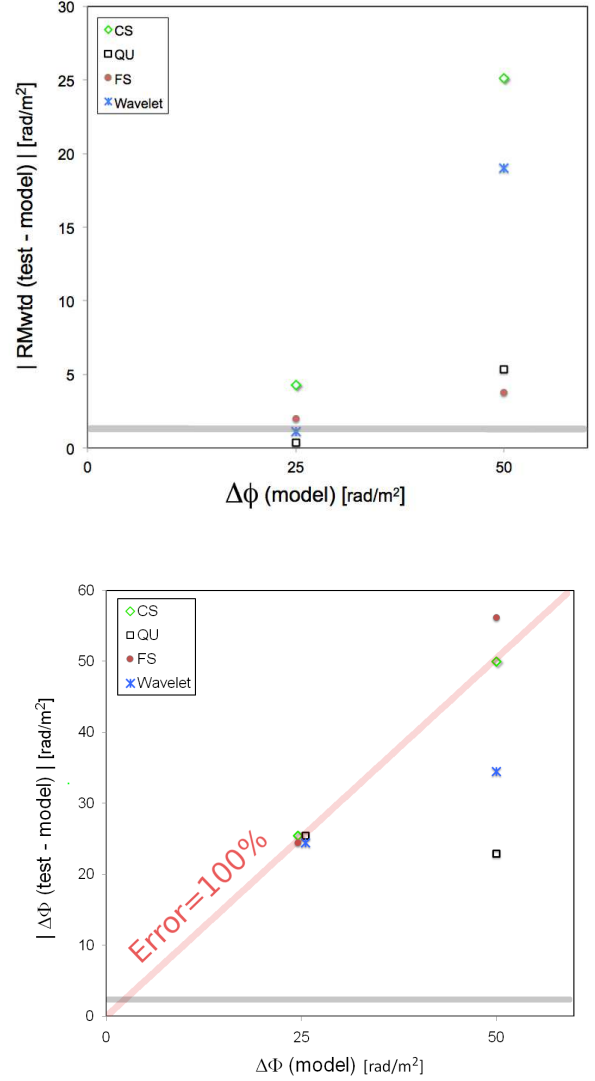


FIG. 5.— Similar as Fig. 4 but for the Faraday thick model.

is larger than $\Delta\phi_{\text{FPSF}}$, reaching more than an order of magnitude worse than expected. The reason is unclear. More tests covering a full range of amplitude ratio and phase difference are needed to investigate this. For $\Delta\phi$ values smaller than the $\Delta\phi_{\text{FPSF}}$, QU -fitting produces results that are about a factor of two better than other algorithms.

Turning now to measurements of $\Delta\phi$ itself, QU -fitting results generally identify the existence of more than a single Faraday thin component, but deviate from the input model significantly more than expected theoretically. This is likely an irreducible error introduced by the multiple degrees of freedom in the fits, as discussed below. At values of $\Delta\phi$ much smaller than $\Delta\phi_{\text{FPSF}}$, all the methods including QU -fitting have 100% errors, and this is likely limited by the current bandwidth of 300 MHz. At larger values of $\Delta\phi$ but still less than $\Delta\phi_{\text{FPSF}}$, the other methods still produce 100% errors indicating that they are unable to identify the existence of two components. At even larger separations of $\Delta\phi_{\text{FPSF}} < \Delta\phi \lesssim 1.5\Delta\phi_{\text{FPSF}}$, Faraday synthesis and wavelet algorithms at least recognize the two components, but do a poor job of measuring their separations compared to QU -fitting. Actually

the Faraday synthesis method could fail to identify the two components if the intensity ratio of the two components is much smaller than that in the current tests (Kumazaki *et al.* 2014).

For tests with Faraday thick components, the $|\text{RM}_{\text{wtd}}(\text{test} - \text{model})|$ and $|\Delta\phi(\text{test} - \text{model})|$ against the model $\Delta\phi$ are shown in Fig. 5. QU -fitting produces an RM_{wtd} consistent with the theoretical expectation for $\Delta\phi = 25 \text{ rad m}^{-2}$. For $\Delta\phi = 50 \text{ rad m}^{-2}$, Faraday synthesis is slightly better than QU -fitting but both produce RM_{wtd} deviating largely from the input. For the measurements of $\Delta\phi$, all the methods fail to correctly recognize the thick component when $\Delta\phi = 25 \text{ rad m}^{-2}$. For $\Delta\phi = 50 \text{ rad m}^{-2}$, all the methods are able to identify the thick component, although they cannot reproduce $\Delta\phi$ properly.

4.3. Extended tests with QU -fitting methods

A series of more demanding two component tests was run with lower SNR and smaller $\Delta\phi$. These tests were run only with QU -fitting methods, because of their low χ_r^2 in the experiments described above. The series consisted of eight tests, each with two components of equal polarized and equal total intensity amplitudes. These parameters were known to each participant prior to the fitting. The SNR is 15 for each component, which is still at least a factor of 1.5 higher than envisioned for, e.g., the POSSUM detection limits (e.g. George *et al.* 2012).

Two of the QU -fitting methods (QU-SO'S and QU-AS) used here were described as before. In the time between the two rounds of tests, three additional QU -fitting routines became available. First is QU-SI¹², which uses a MCMC algorithm similar to QU-AS. The second new routine is RMFIT in AIPS, written by E. Greisen (NRAO), which is an interactive Levenberg-Marquardt, non-linear least squared minimization program working pixel by pixel on QU frequency cubes. The number of components to be fit is specified beforehand (two in this case) and optional starting guesses can be made based on the Faraday spectrum. This method is designated QU-LR as the tests were run by L. Rudnick. Finally, the third new routine is QU-JB¹³, which uses MultiNest (Feroz and Hobson 2008; Feroz *et al.* 2009), a library implementing a nested sampling algorithm. This algorithm iteratively selects more closely-clustered points around identified peaks in the likelihood/posterior distribution, which makes it more robust against multimodal distributions or curving degeneracies than traditional MCMC methods (although the test cases here generally did not appear to possess these properties). It calculates the local evidence for Bayesian model selection purposes, but for these extended tests the models were known, so it was used simply to calculate the maximum-likelihood fit, and should produce similar results to any other maximum-likelihood QU -fitting method.

The results are shown in Table 4. The χ_r^2 values for all the tests are very close to 1 and are not listed in the table. The weighted RM averages are close to the input values, with a median difference of 4 rad m^{-2} , within the expected errors. On the other hand, there are some very large differences between the fits and the models,

TABLE 4
RESULTS FROM QU -FITTING METHODS FOR THE EXTENDED TESTS WITH SNR 15 AND MODEL $\Delta\phi = 20, 40 \text{ rad m}^{-2}$. SUMMARY PERFORMANCE OF THE VARIOUS METHODS ACCORDING TO THE ADOPTED FIGURES OF MERIT: RM_{wtd} AND $\Delta\phi$.

	Model	QU-LR	QU-SI	QU-SO'S	QU-AS	QU-JB
RM_{wtd} rad m^{-2}	-140	-138	-146	-138	-138	-138
	-140	-136	-145	-136	-136	-135
	-160	-165	-156	-164	-165	-166
	-160	-163	-152	-151	-162	-162
	-10	-7	19	-10	-6	-6
	180	155	182	187	188	186
	180	181	181	157	181	182
	110	110	112	110	111	111
$\Delta\phi$ rad m^{-2}	20	80	85	80	80	81
	20	23	77	28	23	30
	20	24	33	19	19	26
	20	62	6	20	61	61
	40	43	286	25	43	43
	40	216	44	24	25	25
	40	46	36	54	45	42
	40	41	22	41	30	45

but with no obvious signature in the χ_r^2 values to show if the fit is inappropriate. The difference in the separation between the two fit components are also typically in good agreement with the model, but again, with occasional large discrepancies and no indication of high χ_r^2 . These discrepancies have an important effect when considering the reliability of derived Faraday parameters, and are discussed in more detail in Sect. 5.

5. DISCUSSION

The studies of magnetic fields in foreground Galactic and intergalactic plasmas rely on properly determined values for RM_{wtd} . The scatter in RM_{wtd} between independent extragalactic sources is a source of noise for such foreground experiments, and only by averaging over large numbers of sources can this number be reduced (see Rudnick and Owen 2014). This, in turn, limits the smallest angular area for which sufficiently reliable average RMs can be determined. It is therefore critical that the errors for determining RM_{wtd} are much less than the intrinsic scatter between sources.

In a sample of 37 extragalactic sources, Law *et al.* (2011) used Faraday synthesis and found that $\sim 25\%$ of them had more than a single Faraday component. Given our results that Faraday synthesis often misses composite structure, this must be considered a very conservative lower limit. Gießübel *et al.* (2013) also showed that a large fraction of the sources observed towards M 31 has composite Faraday spectra. Farnes *et al.* (2014) has recently compiled a catalog containing about 1000 extragalactic sources with fraction polarization measured at more than 2 independent frequencies, and a large majority of these sources shows depolarization behavior indicating they are composite. Wherever there is Faraday complexity, only QU -fitting methods will produce results that do not introduce extraneous scatter in RM_{wtd} , given the algorithms available today. It is important to note that these conclusions all apply where λ_{max}^2 is only 1.6 times λ_{min}^2 and where $\delta\phi$ is often comparable to or less than $\Delta\phi_{\text{FPSF}}$. These are realistic conditions, and important to understand, but results from tests with much broader bandwidths and/or broader Faraday structures

¹² SI=Shinsuke Ideguchi

¹³ JB=Justin Bray

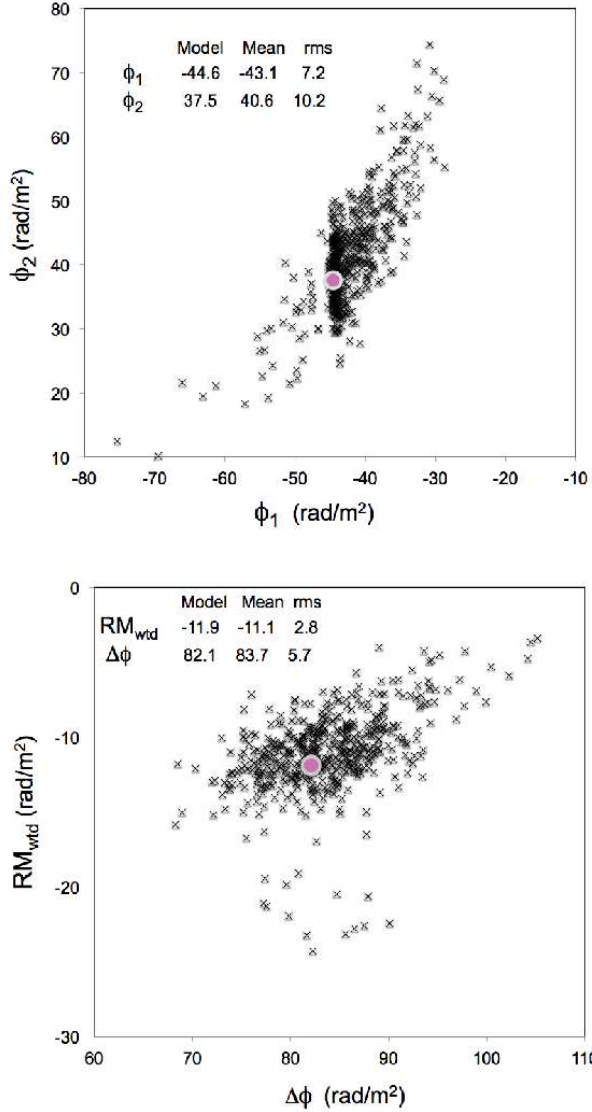


FIG. 6.— QU -fitting results from 500 realizations of a two-component model with $\Delta\phi = 82 \text{ rad m}^{-2}$ and an SNR of about 32. The filled circle indicates the model values. The input values and the mean and 1σ uncertainty of the outputs are also indicated.

would give different results.

For one of the original suite of tests (Model 13, Table 5), and one of the extended, more demanding tests, we performed an additional experiment. We took the same model, and created 500 realizations of the noise, with the same rms, and then fit each of these using QU -JB.

Figure 6 shows the distribution of the values of ϕ_1 and ϕ_2 , along with the model for one test with an input $\Delta\phi \approx 82 \text{ rad m}^{-2}$, somewhat smaller than $\Delta\phi_{\text{FPSF}}$. The scatter in these values is 7.2 rad m^{-2} (10.2 rad m^{-2}), for the stronger (weaker) component, where the expected scatter for these components is only 2 rad m^{-2} (3 rad m^{-2}). The mean values also differ significantly from the input model. However, when we look at the primary measures of scientific interest, RM_{wtd} and $\Delta\phi$ (Fig. 6), we find these are much closer to the input models, with rms scatters of 2.8 and 5.7 rad m^{-2} but still larger than the theoretical values of 1.7 and 4.3 rad m^{-2} .

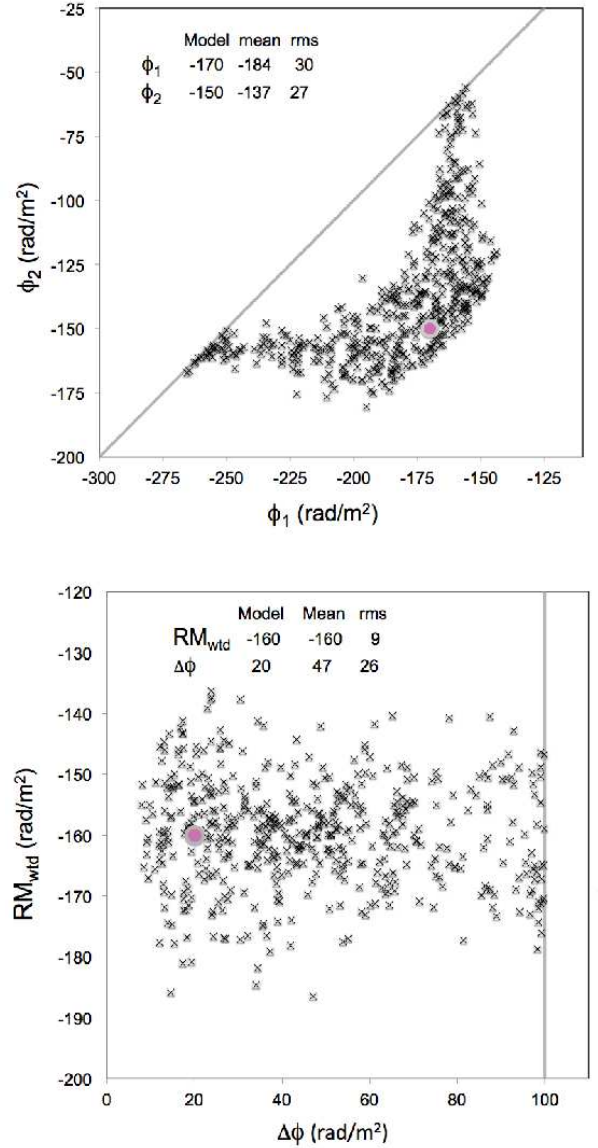


FIG. 7.— The same as Fig. 6 but for the extended test with a component separation of $\Delta\phi = 20 \text{ rad m}^{-2}$ and an SNR of 15.

Performing the same experiment for a second test with an input $\Delta\phi$ of $\sim 20 \text{ rad m}^{-2}$ (Fig. 7), we again see a very large scatter in ϕ_1 and ϕ_2 , 30 and 27 rad m^{-2} , where only 4 rad m^{-2} was expected. We artificially constrained the solutions so that $\Delta\phi < 100 \text{ rad m}^{-2}$, indicated by the grey line, otherwise the actual scatter would be even larger. Looking now at the RM_{wtd} (Fig. 7), the solution is again more reasonable, with a scatter of only 9 rad m^{-2} , where 3 rad m^{-2} was expected. Note that in none of these cases, however, do we approach the theoretical accuracy.

The situation is even worse when we look at $\Delta\phi$. Now we find a very broad range in possible values, and the mean is completely different from the input model. Again, we note the artificial cutoff at $\Delta\phi < 100 \text{ rad m}^{-2}$. The reason for this very large scatter in $\Delta\phi$ can be seen in the plot of q and u versus λ^2 for the data and for two different model fits, shown in Fig. 8. The fact that the q and u curves are almost identical means that these two very different fits cannot be distinguished, virtually inde-

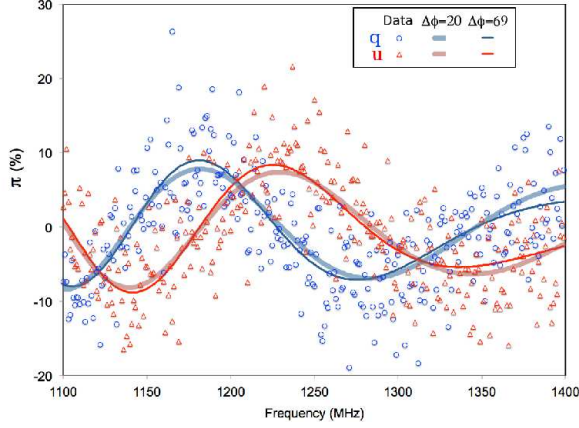


FIG. 8.— Data, input model and an alternative model for one of the extended tests. q (open circles) and u (triangles) are plotted in units of percentage polarization as a function of frequency. The input model (thick lines) has $\Delta\phi=20 \text{ rad m}^{-2}$, while the alternative model (thin lines) has $\Delta\phi=69 \text{ rad m}^{-2}$, yielding approximately the same behaviors of q and u .

pendent of SNR, and independent of the fitting method. The degeneracy is reflected in the data themselves.

The above case presents a fundamental challenge to the accuracy of Faraday measurements. A more thorough investigation with different input phases and amplitudes for the two components are needed to understand the errors for both RM_{wtd} and $\Delta\phi$, and how often extreme cases such as the one above are expected to occur.

6. CONCLUSIONS

We ran a data challenge to benchmark the current available algorithms to reconstruct Faraday spectra. The participating methods included Faraday synthesis and clean, wavelets, compressive sampling, and QU -fitting. The tests were carried out using a 1.1-1.4 GHz band, and signal-to-noise ratios of 32 and 15. Single and double Faraday thin components and Faraday thick components were tested. The figures of merit for these tests consisted of the average Faraday depth weighted by polarized intensity RM_{wtd} , the separation of two Faraday thin components or the extent of a Faraday thick component $\Delta\phi$, and χ_r^2 .

Our main results are:

- Most methods are successful when only one Faraday thin component is present, with occasional failures where two components are found.
- For composite Faraday spectra, the errors in RM_{wtd} are approximately as expected for QU -fitting, and much higher, sometimes by more than an order of magnitude, for all other methods.
- Wherever $\Delta\phi > \Delta\phi_{\text{FPSF}}$, the errors are much larger than expected, with QU -fitting performing the best. At values of $\Delta\phi$ smaller than $\Delta\phi_{\text{FPSF}}$, only QU -fitting reliably recognizes the existence of two components.
- No methods, as currently implemented, work well for Faraday thick components mainly due to the low resolution in the Faraday depth domain given the current narrow bandwidth.

- For certain combinations of input parameters, a wide variety of models are consistent with the same QU data, and therefore no method will be able to accurately determine the true values.

The problems identified above provide a lower limit to the uncertainties for all RM measurements currently in the literature. In fact, the previously published results will often be considerably worse than reported here because the RM determination method, i.e., fitting $\chi(\lambda^2)$ have additional uncertainties (Farnsworth *et al.* 2011). Any results comparing the observed scatter in RMs, for example, to the theoretical uncertainties, will overestimate the contributions to the scatter from the sources themselves.

These results have wide-ranging implications for future polarization surveys and their scientific applications. At present, the use of QU -fitting methods allows us to minimize the scatter in derived Faraday parameters and to reliably identify the presence of Faraday complexity. In addition, any attempts to separate observational errors from intrinsic RM variations between sources or from small-scale foreground fluctuations require a much more sophisticated exploration of error distributions than is currently available.

Motivated by the problems found in recovering the Faraday structures, the participants are now trying to improve their methods. We are also developing more sophisticated models of the input $F(\phi)$ by including other depolarization mechanisms (e.g. Farnes *et al.* 2014) to closely represent the true source structures. The ASKAP early science program plans to cover the frequency range from 700 to 1800 MHz, which is much wider than the 300 MHz bandwidth for the data challenge reported here. All the methods will likely perform better in this new case. The GALFACTS survey at the frequency band of 1225 to 1525 MHz is producing polarization images of the Galactic diffuse emission which is Faraday thick. Clearly it is necessary to investigate further how all the methods are improved to reconstruct Faraday thick components. A second data challenge accounting for all the above effects is underway.

We thank Dr. Rainer Beck for suggesting the nomenclatures and Prof. Bryan Gaensler for very helpful comments on the manuscript. XHS was supported by the Australian Research Council through grant FL100100114. LR acknowledges support from the U.S. National Science Foundation through grant AST-1211595 to the University of Minnesota. JSF acknowledges the support of the ARC through grant DP0986386. TA and KK acknowledge the supports of the Japan Society for the Promotion of Science (JSPS). TO'B acknowledges support from the U.S. National Science Foundation Research Experience for Undergraduates grant to the School of Physics and Astronomy at the University of Minnesota. AS and JB gratefully acknowledge support from the European Research Council under grant ERC-2012-StG-307215 LODESTONE. SPO'S acknowledges the support of the Australian Research Council through grant FS100100033. RS acknowledges support from the grant YD-520.2013.2 and benefited from the International Research Group Program conducted by the Perm region government. RJW is supported by NASA

through the Einstein Postdoctoral grant number PF2-130104 awarded by the Chandra X-ray Center, which is operated by the Smithsonian Astrophysical Observatory

for NASA under contract NAS8-03060. We acknowledge the assistance of Terry Thibault, of the Minnesota Institute for Astrophysics, in blinding the tests for the participants.

REFERENCES

- B. M. Gaensler, R. Beck, and L. Feretti, *NewAR*, **48**, 1003 (2004), [astro-ph/0409100](#).
- L. Harvey-Smith, G. J. Madsen, and B. M. Gaensler, *ApJ*, **736**, 83 (2011), [arXiv:1106.0931 \[astro-ph.GA\]](#).
- A. S. Hill, S. A. Mao, R. A. Benjamin, F. J. Lockman, and N. M. McClure-Griffiths, *ApJ*, **777**, 55 (2013), [arXiv:1309.2553 \[astro-ph.GA\]](#).
- X. H. Sun, W. Reich, C. Wang, J. L. Han, and P. Reich, *A&A*, **535**, A64 (2011), [arXiv:1108.4156 \[astro-ph.GA\]](#).
- J. L. Han, R. N. Manchester, E. M. Berkhuysen, and R. Beck, *A&A*, **322**, 98 (1997).
- X. H. Sun and W. Reich, *RAA*, **10**, 1287 (2010), [arXiv:1010.4394 \[astro-ph.GA\]](#).
- M. Wolleben, A. Fletcher, T. L. Landecker, E. Carretti, J. M. Dickey, B. M. Gaensler, M. Haverkorn, N. McClure-Griffiths, W. Reich, and A. R. Taylor, *ApJ*, **724**, L48 (2010a), [arXiv:1011.0341 \[astro-ph.GA\]](#).
- M. S. Pshirkov, P. G. Tinyakov, P. P. Kronberg, and K. J. Newton-McGee, *ApJ*, **738**, 192 (2011), [arXiv:1103.0814 \[astro-ph.GA\]](#).
- C. L. Van Eck, J. C. Brown, J. M. Stil, K. Rae, S. A. Mao, B. M. Gaensler, A. Shukurov, A. R. Taylor, M. Haverkorn, P. P. Kronberg, and N. M. McClure-Griffiths, *ApJ*, **728**, 97 (2011), [arXiv:1012.2938 \[astro-ph.GA\]](#).
- R. Jansson and G. R. Farrar, *ApJ*, **757**, 14 (2012), [arXiv:1204.3662 \[astro-ph.GA\]](#).
- T. Akahori, D. Ryu, J. Kim, and B. M. Gaensler, *ApJ*, **767**, 150 (2013), [arXiv:1303.1595 \[astro-ph.GA\]](#).
- J. L. Han, R. Beck, and E. M. Berkhuysen, *A&A*, **335**, 1117 (1998), [astro-ph/9805023](#).
- B. M. Gaensler, M. Haverkorn, L. Staveley-Smith, J. M. Dickey, N. M. McClure-Griffiths, J. R. Dickel, and M. Wolleben, *Science*, **307**, 1610 (2005), [arXiv:astro-ph/0503226](#).
- S. A. Mao, N. M. McClure-Griffiths, B. M. Gaensler, M. Haverkorn, R. Beck, D. McConnell, M. Wolleben, S. Stanimirović, J. M. Dickey, and L. Staveley-Smith, *ApJ*, **759**, 25 (2012), [arXiv:1209.1115 \[astro-ph.GA\]](#).
- M. L. Bernet, F. Miniati, and S. J. Lilly, *ApJ*, **772**, L28 (2013), [arXiv:1307.2250 \[astro-ph.CO\]](#).
- A. Bonafede, F. Vazza, M. Brüggen, M. Murgia, F. Govoni, L. Feretti, G. Giovannini, and G. Ogrean, *MNRAS*, **433**, 3208 (2013), [arXiv:1305.7228 \[astro-ph.CO\]](#).
- T. Akahori and D. Ryu, *ApJ*, **723**, 476 (2010), [arXiv:1009.0570 \[astro-ph.CO\]](#).
- T. Akahori and D. Ryu, *ApJ*, **738**, 134 (2011), [arXiv:1107.0142 \[astro-ph.CO\]](#).
- T. Akahori, K. Kumazaki, K. Takahashi, and D. Ryu, *PASJ*, **66**, 65 (2014), [arXiv:1403.0325 \[astro-ph.CO\]](#).
- A. R. Taylor, J. M. Stil, and C. Sunstrum, *ApJ*, **702**, 1230 (2009).
- J. J. Condon, W. D. Cotton, E. W. Greisen, Q. F. Yin, R. A. Perley, G. B. Taylor, and J. J. Broderick, *AJ*, **115**, 1693 (1998).
- D. Farnsworth, L. Rudnick, and S. Brown, *AJ*, **141**, 191 (2011), [arXiv:1103.4149 \[astro-ph.CO\]](#).
- S. P. O'Sullivan, S. Brown, T. Robishaw, D. H. F. M. Schnitzeler, N. M. McClure-Griffiths, I. J. Feain, A. R. Taylor, B. M. Gaensler, T. L. Landecker, L. Harvey-Smith, and E. Carretti, *MNRAS*, **421**, 3300 (2012), [arXiv:1201.3161 \[astro-ph.CO\]](#).
- R. Kothes and J.-A. Brown, in *IAU Symposium*, IAU Symposium, Vol. 259, edited by K. G. Strassmeier, A. G. Kosovichev, and J. E. Beckman (2009) pp. 75–80, [arXiv:0812.3392](#).
- L. Harvey-Smith, B. M. Gaensler, R. Kothes, R. Townsend, G. H. Heald, C.-Y. Ng, and A. J. Green, *ApJ*, **712**, 1157 (2010), [arXiv:1001.3462 \[astro-ph.GA\]](#).
- M. Haverkorn, P. Katgert, and A. G. de Bruyn, *A&A*, **404**, 233 (2003), [arXiv:astro-ph/0304087](#).
- D. H. F. M. Schnitzeler, P. Katgert, and A. G. de Bruyn, *A&A*, **494**, 611 (2009), [arXiv:0810.4211](#).
- R. Braun, G. Heald, and R. Beck, *A&A*, **514**, A42 (2010), [arXiv:1002.1776 \[astro-ph.CO\]](#).
- A. Fletcher, R. Beck, A. Shukurov, E. M. Berkhuysen, and C. Horellou, *MNRAS*, **412**, 2396 (2011), [arXiv:1001.5230 \[astro-ph.CO\]](#).
- S. P. O'Sullivan, I. J. Feain, N. M. McClure-Griffiths, R. D. Ekers, E. Carretti, T. Robishaw, S. A. Mao, B. M. Gaensler, J. Bland-Hawthorn, and L. Stawarz, *ApJ*, **764**, 162 (2013), [arXiv:1301.1400 \[astro-ph.CO\]](#).
- A. Brandenburg and R. Stepanov, *ApJ*, **786**, 91 (2014), [arXiv:1401.4102](#).
- C. Horellou and A. Fletcher, *MNRAS*, **441**, 2049 (2014), [arXiv:1401.4152](#).
- B. J. Burn, *MNRAS*, **133**, 67 (1966).
- D. D. Sokoloff, A. A. Bykov, A. Shukurov, E. M. Berkhuysen, R. Beck, and A. D. Poezd, *MNRAS*, **299**, 189 (1998).
- M. Wolleben, T. L. Landecker, G. J. Hovey, R. Messing, O. S. Davison, N. L. House, K. H. M. S. Somaratne, and I. Tashev, *AJ*, **139**, 1681 (2010b), [arXiv:1002.2312 \[astro-ph.IM\]](#).
- A. R. Taylor and C. J. Salter, in *The Dynamic ISM: A Celebration of the Canadian Galactic Plane Survey*, Astronomical Society of the Pacific Conference Series, Vol. 438, edited by R. Kothes, T. L. Landecker, & A. G. Willis (2010) p. 402, [arXiv:1008.4944 \[astro-ph.IM\]](#).
- B. M. Gaensler, T. L. Landecker, A. R. Taylor, and POSSUM Collaboration, in *American Astronomical Society Meeting Abstracts #215*, Bulletin of the American Astronomical Society, Vol. 42 (2010) p. 470.13.
- M. A. Brentjens and A. G. de Bruyn, *A&A*, **441**, 1217 (2005), [arXiv:astro-ph/0507349](#).
- G. Heald, in *IAU Symposium*, IAU Symposium, Vol. 259 (2009) pp. 591–602.
- M. R. Bell and T. A. Enßlin, *A&A*, **540**, A80 (2012), [arXiv:1112.4175 \[astro-ph.IM\]](#).
- K. Kumazaki, T. Akahori, S. Ideguchi, T. Kurayama, and K. Takahashi, *PASJ*, **66**, 61 (2014), [arXiv:1402.0612 \[astro-ph.IM\]](#).
- P. Frick, D. Sokoloff, R. Stepanov, and R. Beck, *MNRAS*, **401**, L24 (2010), [arXiv:0911.0261 \[astro-ph.GA\]](#).
- P. Frick, D. Sokoloff, R. Stepanov, and R. Beck, *MNRAS*, **414**, 2540 (2011), [arXiv:1102.4316 \[astro-ph.GA\]](#).
- F. Li, S. Brown, T. J. Cornwell, and F. de Hoog, *A&A*, **531**, A126 (2011), [arXiv:1106.1709 \[astro-ph.IM\]](#).
- M. Andrecut, J. M. Stil, and A. R. Taylor, *AJ*, **143**, 33 (2012), [arXiv:1111.4167 \[astro-ph.CO\]](#).
- S. Ideguchi, K. Takahashi, T. Akahori, K. Kumazaki, and D. Ryu, *PASJ*, **66**, 5 (2014), [arXiv:1308.5696 \[astro-ph.CO\]](#).
- J. A. Högbom, *A&AS*, **15**, 417 (1974).
- M. R. Bell, N. Oppermann, A. Crai, and T. A. Enßlin, *A&A*, **551**, L7 (2013), [arXiv:1211.5105 \[astro-ph.IM\]](#).
- R. Beck, P. Frick, R. Stepanov, and D. Sokoloff, *A&A*, **543**, A113 (2012), [arXiv:1204.5694 \[astro-ph.IM\]](#).
- A. M. M. Scaife and G. H. Heald, *MNRAS*, **423**, L30 (2012), [arXiv:1203.0977 \[astro-ph.IM\]](#).
- S. J. George, J. M. Stil, and B. W. Keller, *PASA*, **29**, 214 (2012), [arXiv:1106.5362 \[astro-ph.IM\]](#).
- A. H. Minter and S. R. Spangler, *ApJ*, **458**, 194 (1996).
- S. A. Mao, B. M. Gaensler, M. Haverkorn, E. G. Zweibel, G. J. Madsen, N. M. McClure-Griffiths, A. Shukurov, and P. P. Kronberg, *ApJ*, **714**, 1170 (2010), [arXiv:1003.4519 \[astro-ph.GA\]](#).
- X. H. Sun and W. Reich, *A&A*, **507**, 1087 (2009), [arXiv:0908.3378](#).
- D. H. F. M. Schnitzeler, *MNRAS*, **409**, L99 (2010), [arXiv:1011.0737 \[astro-ph.GA\]](#).
- F. Feroz and M. P. Hobson, *MNRAS*, **384**, 449 (2008), [arXiv:0704.3704](#).
- F. Feroz, M. P. Hobson, and M. Bridges, *MNRAS*, **398**, 1601 (2009), [arXiv:0809.3437](#).

L. Rudnick and F. N. Owen, ApJ, **785**, 45 (2014),
arXiv:1402.3637.

C. J. Law, B. M. Gaensler, G. C. Bower, D. C. Backer,
A. Bauermeister, S. Croft, R. Forster, C. Gutierrez-Kraybill,
L. Harvey-Smith, C. Heiles, C. Hull, G. Keating,
D. MacMahon, D. Whyson, P. K. G. Williams, and
M. Wright, ApJ, **728**, 57 (2011),
arXiv:1012.0945 [astro-ph.CO].
R. Gießbübel, G. Heald, R. Beck, and T. G. Arshakian, A&A,
559, A27 (2013), arXiv:1309.2539 [astro-ph.CO].
J. S. Farnes, B. M. Gaensler, and E. Carretti, ApJS, **212**, 15
(2014), arXiv:1403.2391

TABLE 5
INPUT MODELS AND RESULTS FOR THE DATA CHALLENGE.

	Thin component 1			Thin component 2			Thick component			RM _{wtd} rad m ⁻²	χ _r ²
	p ₁ %	φ ₁ rad m ⁻²	χ ₁ °	p ₂ %	φ ₂ rad m ⁻²	χ ₂ °	p ₀ %	φ _c rad m ⁻²	φ _s rad m ⁻²		
<i>One Faraday thin component</i>											
Model 1	100.00	500.10	40.00							500.1	0.98
FS-JF	95.77	501.58	37.01							501.6	0.99
FS-KK	27.30	500.60	40.50							500.6	1.76
FS-LR	90.00	502.00	79.00							502.0	3.04
FS-MB	95.60	501.2	37.3							501.2	0.99
FS-MBn	95.60	501.6	37.4							501.6	0.99
FS-MW	90.40	501.00	82.00	7.90	-387.50	12.00				429.6	3.95
FS-RvW								400.00		400.0	
Wavelet-RS	13.00	499.00	42.00							499.0	2.12
CS-JS	88.20	502.20	35.00							502.2	1.00
CS-XS	61.54	496.12	45.00	10.80	498.02	45.00				496.4	1.25
QU-AS	95.60	500.81	37.18							500.8	0.98
QU-SO'S	96.00	501.4	37.5							501.4	0.99
QU-TO'B	95.82	501.52	37.22							501.5	0.99
Model 2	100.00	49.38	60.00							49.4	1.02
FS-JF	96.20	52.35	50.20							52.4	1.02
FS-KK	27.60	52.70	49.00							52.7	1.81
FS-LR	91.00	52.50	50.00							52.5	1.02
FS-MB	96.15	52.2	50.8							52.2	1.02
FS-MBn	96.70	52.7	49.0							52.7	1.02
FS-MW	92.30	50.50	-4.90							50.5	5.56
FS-RvW		50.00								50.0	
Wavelet-RS	13.00	52.00	50.00							52.0	2.18
CS-JS	89.60	52.60	48.80							52.6	1.03
CS-XS	42.83	51.52	45.00	29.50	38.16	-90.00				46.1	1.22
QU-AS	96.15	52.41	49.85							52.4	1.02
QU-SO'S	96.00	52.3	50.3							52.3	1.02
QU-TO'B	96.44	52.35	50.28							52.3	1.02
Model 3	100.00	4.96	60.00							5.0	0.97
FS-JF	104.53	5.35	59.27							5.4	0.97
FS-KK	29.30	5.80	58.00							5.8	1.90
FS-LR	95.00	5.00	120.00							5.0	5.90
FS-MB	106.04	4.6	61.6							4.6	0.97
FS-MBn	104.40	5.0	60.3							5.0	0.97
FS-MW	102.00	4.00	-33.60							4.0	7.95
FS-RvW		0.00								0.0	
Wavelet-RS	15.00	6.00	57.00							6.0	2.30
CS-JS							124.00	4.57	18.30	4.6	0.98
CS-XS	72.85	7.63	45.00	15.99	-5.72	90.00				5.2	1.09
QU-AS	104.95	5.30	-120.53							5.3	0.97
QU-SO'S	11.50	6.3	56.3							6.3	0.98
QU-TO'B	104.63	5.40	59.12							5.4	0.97
<i>Two Faraday thin components</i>											
Model 4	25.00	-37.84	0.00	16.7	103.18	-36.00				18.6	0.97
FS-JF	28.83	-43.01	16.17	21.68	112.36	-67.31				23.7	1.12
FS-KK	32.90	-43.70	19.50	17.20	111.40	-64.50				9.5	1.14
FS-LR	24.00	-41.50	14.00	13.00	111.10	-63.80				12.1	1.00
FS-MB	24.31	-47.4	31.5	1.09	121.4	-99.0				-40.2	1.58
FS-MBn	24.86	-47.4	31.7	1.11	121.4	-99.3				-40.1	1.56
FS-MW	23.10	-49.10	-3.00	15.20	95.70	-90.00				8.4	6.92
FS-RvW		-50.00			-100.00	0.00					
Wavelet-RS	14.00	-44.00	19.00	8.00	112.00	-69.00				12.7	1.58
CS-JS	21.50	-42.80	15.10	12.60	111.40	-64.40				14.2	1.04
CS-XS	14.57	-40.07	0.00	7.16	-53.43	45.00				-44.5	1.19
QU-AS	25.3	-34.64	12.67	16.07	98.95	-22.82				17.3	2.16
QU-SO'S	25.00	-40.7	8.6	16.00	108.2	-54.1				17.4	0.96
QU-TO'B	25.24	-40.70	8.72	15.90	108.22	-44.85				16.9	1.04
Model 5	25.00	-37.84	-40.00	24.00	5.05	-40.00				-16.8	1.01
FS-JF	38.70	-13.65	39.62							-13.7	1.25
FS-KK	47.20	-13.80	40.50							-13.8	1.42
FS-LR	28.00	-13.75	39.50				6.00	-19.00	92.00	-13.8	1.60
FS-MB	39.32	-13.5	39.3							-13.5	1.25
FS-MBn	39.45	-13.2	38.4							-13.2	1.25
FS-MW	35.60	-14.50	-128.00							-14.5	1.68
FS-RvW		-50.00								-50.0	
Wavelet-RS	12.00	-31.00	-71.00	4.00	-70.00	-84.00	17.00	-14.00	97.00	-14.0	5.20
CS-JS	29.10	-13.40	39.00	3.70	34.30	34.40				-8.0	1.38
CS-XS	23.45	-5.72	0.00	11.05	-51.52	0.00				-20.4	1.50
QU-AS	29.7	-37.57	-13.21	49.52	-14.16	-155.45				-22.9	1.00
QU-SO'S	24.00	-37.0	-40.4	28.00	3.4	-34.6				-15.2	0.99
QU-TO'B	25.07	-36.50	-39.88	30.04	2.30	-32.23				-15.3	1.00
Model 6	25.00	-37.84	-40.00	9.00	5.05	-40.00				-26.5	1.00
FS-JF	27.38	-31.25	-69.52							-31.3	1.06
FS-KK	32.90	-30.80	-70.50							-30.8	1.13
FS-LR	22.00	-31.50	-68.00				3.00	-16.00	102.00	-31.5	1.16
FS-MB	27.81	-33.1	-63.6							-33.1	1.06
FS-MBn	27.81	-31.9	-67.7							-31.9	1.06
FS-MW	26.90	-34.30	42.00	2.00	-648.00	-27.00				-76.8	8.74
FS-RvW		-50.00								-50.0	
Wavelet-RS	12.00	-31.00	-71.00	4.00	-70.00	-84.00				-40.8	1.62
CS-JS	22.70	-31.00	-69.80							-31.0	1.13
CS-XS	11.03	-40.07	-45.00	7.61	-51.52	0.00				-44.7	1.38
QU-AS	27.1	-35.17	-48.75	9.17	12.83	-76.14				-23.0	1.00

TABLE 5 — *Continued*

	Thin component 1			Thin component 2			Thick component			RM _{wtg} rad m ⁻²	χ_r^2
	p_1 %	ϕ_1 rad m ⁻²	χ_1 °	p_2 %	ϕ_2 rad m ⁻²	χ_2 °	p_0 %	ϕ_c rad m ⁻²	ϕ_s rad m ⁻²		
QU-SO'S	26.00	-38.0	-40.8	8.00	12.9	-68.3				-26.0	1.00
QU-TO'B	25.43	-38.15	-38.41	9.47	7.88	-52.57				-25.7	1.00
Model 7	25.00	-44.55	0.00	16.70	37.50	72.00				-11.7	1.01
FS-JF	32.41	-17.55	86.09							-17.6	1.13
FS-KK	37.80	-16.40	82.50							-16.4	1.21
FS-LR	28.00	-17.50	85.00							-17.5	1.19
FS-MB	33.65	-18.8	90.2							-18.8	1.14
FS-MBn	33.52	-18.3	88.4							-18.3	1.14
FS-MW	30.70	-22.60	19.00							-22.6	11.62
FS-RvW		-10.00								-10.0	
Wavelet-RS	15.00	-16.00	82.00							-16.0	1.94
CS-JS	25.50	-18.00	86.50							-18.0	1.23
CS-XS	23.21	-7.63	45.00	6.92	-72.51	90.00				-22.5	1.27
QU-AS	31.04	-29.86	-51.04	9.60	66.48	147.90				-7.1	1.01
QU-SO'S	28.00	-38.0	-22.0	13.00	46.2	40.6				-11.3	1.00
QU-TO'B	28.28	-36.99	-25.66	12.33	47.23	36.69				-11.4	1.00
Model 8	25.00	232.56	40.00	9.00	192.70	40.00				222.0	0.97
FS-JF	26.04	230.76	55.23							230.8	1.06
FS-KK	31.20	230.30	56.50							230.3	1.12
FS-LR	19.00	231.00	55.00							231.0	1.19
FS-MB	26.10	231.0	54.7							231.0	1.06
FS-MBn	26.37	231.3	53.6							231.3	1.06
FS-MW	23.30	229.50	95.00	2.00	-649.00	36.00				160.1	3.36
FS-RvW								200.00		200.0	
Wavelet-RS	11.00	230.00	58.00							230.0	1.66
CS-JS	19.90	231.00	59.00							231.0	1.16
CS-XS	9.04	230.89	45.00	7.90	255.69	-45.00				232.5	1.16
QU-AS	22.00	242.18	-173.22	10.85	192.45	28.51				225.7	0.96
QU-SO'S	22.00	243.6	3.4	11.00	190.6	34.3				225.9	0.96
QU-TO'B	26.33	231.47	52.73	3.47	10.40	38.94				205.7	1.03
Model 9	25.00	-37.83	-40.00	16.50	5.05	140.00				-20.8	0.99
FS-JF	31.61	-21.85	-106.88							-21.9	1.19
FS-KK	38.80	-21.10	-109.00							-21.1	1.31
FS-LR	24.00	-22.00	-106.50							-22.0	1.36
FS-MB	32.19	-22.6	-104.3							-22.6	1.19
FS-MBn	32.47	-22.5	-104.3							-22.5	1.19
FS-MW	29.30	-28.50	46.70							-28.5	7.07
FS-RvW		-25.00	0.00							-25.0	
Wavelet-RS	14.00	-21.00	-110.00							-21.0	2.06
CS-JS	23.40	-21.90	-107.30	3.84	-57.80	32.60				-27.0	1.26
CS-XS							6.00	-22.00	56.00	-22.0	1.31
QU-AS	34.50	-24.82	98.03	19.56	7.89	-67.95				-13.0	0.98
QU-SO'S	30.00	-29.1	-69.7	16.00	10.7	-70.9				-15.2	0.98
QU-TO'B	31.62	-28.35	-70.22	18.46	8.27	-64.39				-14.8	0.98
Model 10	25.00	-37.84	0.00	9.00	103.00	-36.00				-0.6	1.08
FS-JF	26.35	-40.25	8.07	14.78	115.25	-77.72				15.6	1.19
FS-KK	30.00	-41.10	10.50	9.65	109.50	121.50				-4.4	1.17
FS-LR	23.00	-39.00	6.00	6.50	112.00	-65.00				-5.7	1.12
FS-MB	23.63	-41.6	12.8	0.60	120.1	82.8				-37.6	1.27
FS-MBn	23.90	-41.7	13.4	0.61	125.0	68.5				-37.6	1.27
FS-MW	22.50	-45.00	-4.00	7.70	103.00	89.00				-7.3	3.17
FS-RvW		-50.00									
Wavelet-RS	14.00	-41.00	11.00	3.00	113.00	-69.00				-13.8	1.54
CS-JS	23.20	-40.20	7.20	6.08	112.10	23.70				-8.6	1.71
CS-XS	15.92	-40.07	0.00	4.83	-38.16	-0.01				-39.6	1.44
QU-AS	24.18	-37.73	179.57	9.50	105.66	131.91				2.7	1.08
QU-SO'S	24.00	-37.0	-3.0	9.00	102.4	-36.2				1.0	0.98
QU-TO'B	24.49	-36.59	-4.34	9.20	100.81	-30.84				0.9	1.07
Model 11	25.00	149.50	40.00	23.75	163.50	-68.00				156.3	1.16
FS-JF	21.66	153.86	-2.09							153.9	1.17
FS-KK	25.70	154.20	-3.00							154.2	1.21
FS-LR	17.00	153.75	-2.00							153.8	1.23
FS-MB	21.84	152.6	2.3							152.6	1.17
FS-MBn	21.84	153.6	-1.3							153.6	1.17
FS-MW	21.20	144.50	57.80	2.0	-800.00	-155.60				63.1	2.30
FS-RvW		150.00			250.00						
Wavelet-RS	10.00	154.00	-3.00							154.0	1.53
CS-JS	18.20	153.20	0.00							153.2	1.20
CS-XS	13.74	139.29	45.00	6.38	187.00	-135.00				154.4	1.24
QU-AS	21.70	153.40	178.74							153.4	1.17
QU-SO'S	17.00	143.1	46.9	11.00	175.8	-98.5				155.9	1.14
QU-TO'B	17.17	143.35	45.27	10.3	177.50	-105.22				155.9	1.14
Model 12	25.00	-232.56	0.00	9.00	-50.10	72.00				-184.3	1.02
FS-JF	25.19	-235.56	9.66							-235.6	1.26
FS-KK	28.60	-234.00	4.00	11.40	-58.30	99.50				-183.9	1.03
FS-LR	19.00	-236.00	8.50	3.90	-51.50	73.00				-204.6	1.24
FS-MB	26.65	-230.4	-9.6	0.76	-72.4	149.9				-226.0	1.27
FS-MBn	26.24	-230.7	-8.2	0.71	-81.2	0.7				-226.8	1.26
FS-MW	25.50	-237.20	-54.00	4.00	-43.30	158.50				-210.9	7.44
FS-RvW		-200.00			0.00						
Wavelet-RS	13.00	-233.00	0.00	4.00	-74.00	-28.00				-195.6	1.56
CS-JS	16.50	-235.60	16.50							-235.6	1.51
CS-XS	22.83	-234.70	0.00	6.05	-57.24	90.00				-197.5	1.17
QU-AS	26.80	-231.82	-2.98	9.89	-61.57	-68.58				-185.9	1.01
QU-SO'S	27.00	-231.6	-5.5	10.00	-58.7	100.5				-184.8	1.01
QU-TO'B	26.66	-231.52	-5.60	10.21	-58.74	100.64				-183.7	1.01
Model 13	25.00	-44.55	0.00	24.00	37.54	72.00				-4.3	0.99
FS-JF	37.88	-4.65	39.67							-4.7	1.22
FS-KK	44.50	-4.80	40.00							-4.8	1.33
FS-LR	26.00	-2.00	78.00							-2.0	7.27
FS-MB	25.82	-5.4	42.6							-5.4	1.61
FS-MBn	25.69	-4.9	40.5							-4.9	1.61
FS-MW	34.60	-13.00	21.20							-13.0	8.70
FS-RvW		0.00								0.0	
Wavelet-RS	17.00	-5.00	40.00							-5.0	2.38
CS-JS	28.80	-4.90	40.40							-4.9	1.44
CS-XS	13.81	-34.35	-45.00	12.83	30.53	90.00				-3.1	1.25
QU-AS	31.7	-28.01	121.79	16.62	55.69	7.18				0.8	0.99
QU-SO'S	27.00	-38.5	-21.1	22.00	41.9	55.9				-2.4	0.98
QU-TO'B	27.08	-38.55	-20.98	21.72	41.89	55.90				-2.7	0.98

TABLE 5 — *Continued*

	Thin component 1			Thin component 2			Thick component			RM _{wtg} rad m ⁻²	χ _r ²
	p ₁ %	φ ₁ rad m ⁻²	χ ₁ °	p ₂ %	φ ₂ rad m ⁻²	χ ₂ °	p ₀ %	φ _c rad m ⁻²	φ _s rad m ⁻²		
Paraday thick component											
Model 14							1.90	-136.98	50.00	-137.0	0.97
FS-JF	6.03	-71.95	34.49	5.71	-210.14	70.24				-139.2	1.09
FS-KK	16.10	-68.90	24.50	12.70	-192.80	18.00				-123.5	4.80
FS-LR							1.00	-117.50	305.00	-117.0	2.11
FS-MB	4.37	-193.1	16.0	0.92	-80.6	58.6				-173.5	1.40
FS-MBn	4.47	-201.7	44.6	0.91	-79.6	54.9				-181.0	1.37
FS-MW	4.00	-211.80	-21.50	5.80	-83.00	82.00				-135.6	2.56
FS-RvW		-75.00			175.00						
Wavelet-RS	7.00	-72.00	34.00				6.00	-140.00	69.00	-103.0	2.01
CS-JS	1.25	-72.20	37.80	0.26	-208.10	63.90				-95.6	1.80
CS-XS	3.99	-74.42	45.00							-74.4	1.05
QU-AS	8.63	-165.85	-82.75	8.90	-114.95	2.33				-139.9	0.93
QU-SO'S	6.00	-206.5	51.0				57.00		70.8	-206.5	1.5
QU-TO'B	0.89	-190.70	-0.09				19.47	-101.40	40.00	-101.0	1.13
Model 15	1.80	-240.22	-36.00				1.90	-250.17	50.00	-245.0	1.03
FS-JF	7.29	-241.56	-31.09							-241.6	1.06
FS-KK	31.30	-241.30	-31.50							-241.3	23.87
FS-LR	5.90	-241.50	-30.50							-241.5	1.13
FS-MB	7.19	-241.9	-30.1							-241.9	1.06
FS-MBn	7.19	-241.2	-32.5							-241.2	1.06
FS-MW	6.60	-259.50	10.00							-259.5	2.02
FS-RvW		-250.00			150.00						
Wavelet-RS	17.00	-241.00	-32.00							-241.0	4.80
CS-JS							10.53	-241.80	24.80	-242.0	1.03
CS-XS	3.38	-253.78	0.00							-253.8	1.18
QU-AS	7.26	-241.30	149.13							-241.3	1.05
QU-SO'S	7.00	-241.6	-30.9							-241.6	1.06
QU-TO'B							10.92	-241.62	25.40	-252.0	1.03
Model 16							1.90	-136.98	25.00	-137.0	
FS-JF	6.67	-139.46	46.91							-139.5	1.03
FS-KK	19.40	-139.20	46.00							-139.2	3.96
FS-LR	5.50	-138.75	46.00							-138.8	1.05
FS-MB	6.63	-139.8	48.2							-139.8	1.03
FS-MBn	6.63	-139.8	48.0							-139.8	1.03
FS-MW	7.40	-152.50	-60.00							-152.5	1.94
FS-RvW		-150.00			-50.00			-250.00			
Wavelet-RS	10.00	-139.00	46.00							-139.0	1.23
CS-JS	5.65	-138.90	45.30							-138.9	1.05
CS-XS	1.99	-141.20	45.00	1.97	-156.47	-90.00				-148.8	1.25
QU-AS	6.68	-138.75	45.25							-138.8	1.03
QU-SO'S	7.00	-139.3	46.2							-139.3	1.03
QU-TO'B	5.71	-144.60	45.00	4.23	-128.27	38.44				-137.6	1.02
Model 17	1.80	-240.00	-36.00				1.90	-250.17	25.00	-245.2	
FS-JF	10.78	-245.36	-18.29							-245.4	0.97
FS-KK	47.40	-244.80	7.50							-244.8	53.95
FS-LR	10.20	-245.00	-18.25							-245.0	0.98
FS-MB	3.02	-245.4	-19.6							-245.4	0.97
FS-MBn	3.02	-245.0	-18.4							-245.0	0.97
FS-MW	9.90	-247.50	-18.50							-247.5	2.52
FS-RvW		-17.80						-250.00			
Wavelet-RS	22.00	-245.00	-18.40							-245.0	5.97
CS-JS	10.40	-245.40	-20.00							-245.4	0.97
CS-XS	5.47	-238.52	-20.00							-238.5	1.20
QU-AS	10.75	-245.11	-18.05							-245.1	0.96
QU-SO'S	11.00	-245.3	-18.4							-245.3	0.97
QU-TO'B	10.79	245.33	0.00							245.3	0.97